Article

Reconstructing Long-Term Arctic Sea Ice Freeboard, Thickness, and Volume Changes from Envisat, CryoSat-2, and ICESat-2

Yanze Zhang [1], Nengfang Chao [1,2,3,*], Fupeng Li [1,4], Lianzhe Yue [1], Shuai Wang [2], Gang Chen [1,2], Zhengtao Wang [5], Nan Yu [1], Runzhi Sun [1] and Guichong Ouyang [2]

[1] College of Marine Science and Technology, China University of Geosciences, Wuhan 430074, China
[2] Key Laboratory of Geological Survey and Evaluation of Ministry of Education, China University of Geosciences, Wuhan 430074, China
[3] Centre for Polar Observation and Modelling, School of Earth and Environment, University of Leeds, Leeds LS2 9JT, UK
[4] Institute of Geodesy and Geoinformation, University of Bonn, 53115 Bonn, Germany
[5] Key Laboratory of Geospace Environment and Geodesy, School of Geodesy and Geomatics, Wuhan University, Wuhan 430079, China
* Correspondence: chaonf@cug.edu.cn

Simple Summary: The rapid decline of Arctic sea ice (ASI) has significantly impacted the global climate, polar ecosystems, and shipping courses. Precise long-term and high-resolution changes in ASI estimates are crucial for adapting to climate change and developing Arctic marine resources. Satellite altimeters have been applied to detect ASI for several decades. However, the mission periods of various altimetry satellites are limited, making it challenging to estimate the long-term change process of ASI thickness from the observations of a single altimetry satellite or simply combining multi-source satellite altimetry data. The purpose of this study is to comprehensively obtain continuous long-term ASI freeboard, thickness, and volume characteristics using the gridded nadirization method from Envisat, CryoSat-2, and ICESat-2 altimeter data. The relationship between surface temperature and surface wind field is also investigated. The freeboard, thickness, extent, and area of ASI consistently showed loss trends during 2002–2021, and sea ice volume decreased by 5437 km^3/month. Sea surface temperature and sea surface wind field are two of the essential influencing factors on ASI variations. This study will assist in clarifying the relationship between climate variations and the ASI decline.

Abstract: Satellite altimeters have been used to monitor Arctic sea ice (ASI) thickness for several decades, but whether the different altimeter missions (such as radar and laser altimeters) are in agreement with each other and suitable for long-term research needs to be investigated. To analyze the spatiotemporal characteristics of ASI, continuous long-term first-year ice, and multi-year ice of ASI freeboard, thickness, and volume from 2002 to 2021 using the gridded nadirization method from Envisat, CryoSat-2, and ICESat-2, altimeter data are comprehensively constructed and assessed. The influences of sea surface temperature (SST) and sea surface wind field (SSW) on ASI are also discussed. The freeboard/thickness and extent/area of ASI all varied seasonally and reached their maximum and minimum in April and October, March and September, respectively. From 2002 to 2021, the freeboard, thickness, extent, and area of ASI all consistently showed downward trends, and sea ice volume decreased by 5437 km^3/month. SST in the Arctic rose by 0.003 degrees C/month, and the sea ice changes lagged behind this temperature variation by one month between 2002 and 2021. The meridional winds blowing from the central Arctic region along the eastern coast of Greenland to the North Atlantic each month are consistent with changes in the freeboard and thickness of ASI. SST and SSW are two of the most critical factors driving sea ice changes. This study provides new data and technical support for monitoring ASI and exploring its response mechanisms to climate change.

Keywords: Envisat/CryoSat-2/ICESat-2; sea ice freeboard and thickness; sea ice volume; arctic sea ice

1. Introduction

Polar sea ice change is an "amplifier" and "indicator" of global climate change, and it has a vital impact on polar circles through oceans, ecosystems, and the atmosphere [1,2]. Arctic sea ice (ASI) is one of the most rapidly changing important factors in the global climate system. ASI extent and thickness have declined significantly over the past few decades [3–5]. ASI coverage affects albedo [6], and its thickness and volume can affect global heat budget [7] and freshwater exchanges [8,9], especially the Fram Strait in the Greenland Sea, which is the predominant channel for exchanging Arctic Ocean water with other oceanic water bodies [10]. ASI also affects the habitat and reproduction of animals [11] and human economic and military activities in the Arctic Circle [12]. Additionally, the cold air temperatures over the Arctic Ocean create conditions that allow for sea ice formation and growth, resulting in ice cover throughout the year with seasonal variability. However, the intensification of global climate change has caused ASI to rapidly melt, having an important impact on global and Arctic sea-level changes, ecosystems, and the safety of human lives and properties. Therefore, long-term and high-resolution sea ice thickness estimations are required [13,14] to accurately assess climate change, sea ice mass balance, and ocean–sea–ice interactions with the atmosphere [15–17].

Traditional methods, such as field ice drilling, aerial observation, electromagnetic induction, and sonar, have difficulty obtaining long-term and large-scale observational data of sea ice thickness. However, with the development of satellite altimetry, it is now possible to procure precise hemispheric observational data on long-term ASI thickness variations. This sea ice is freeboard, that is, it is sea ice that protrudes above the water level, and its total thickness is the combination of this freeboard and the draft, retrieved by satellite altimetry data. These data rely on the identification of leads, which are narrow and linear cracks in ice that form when ice floes diverge or shear as they move parallel to each other. Sea ice thickness is closely related to the estimation of the input parameters of the equation and calculation of the freeboard. Therefore, previous studies have adopted different processing methods for these calculations. For example, Laxon et al. [18] used European Remote Sensing Satellite-1/2 (ERS-1/2) radar satellite data (covering an area of up to ±81.5 degrees latitude) to obtain a surface elevation of floes/leads by investigating the individual echoes and re-tracked the waveform after classifying the echoes into lead or floe to obtain the freeboard, which was then used in the equation for hydrostatic equilibrium to calculate the average winter thickness (approximately 2.73 m) from 1993 to 2001; these results were then verified using submarine thickness data. Overall, these results show that the use of radar satellite altimetry data can effectively obtain large-scale sea ice thickness data. Giles et al. [19] analyzed the echo waveform, distinguished between open water and ice floe, and corrected the time necessary for radar penetrating snow to determine ASI thickness from 2002 to 2007 based on Envisat data. These results showed that the average sea ice thickness diminished by 0.26 m during this period. Furthermore, S. W. Laxon et al. [20] and Tilling et al. [21] used CryoSat-2 data to distinguish sea ice and leads by analyzing echo waveforms and then determined the sea ice freeboard and thickness.

These previous studies used radar satellite altimetry data from the Ice, Cloud, and land Elevation Satellite (ICESat) and ICESat-2. ICESat-2 was equipped with an advanced topographic laser altimeter system (ATLAS), which can provide elevation data with higher spatiotemporal resolutions, providing more reliable data for ASI thickness analysis. Kwok et al. [22] combined ICESat data with RADARSAT synthetic aperture radar (SAR) images to calculate sea ice freeboard, and they used snow climatology to estimate the average thickness of sea ice in northern Ellesmere Island and the East Siberian Sea. Kwok and Cunningham [23] used ICESat data to reconstruct daily snow depths, used moored sonar data for comparison and verification, and conducted a sensitivity analysis on the parameters of the inversion of sea ice thickness. The averaged sea ice thicknesses in February and March 2006 were 2.15 and 2.46 m, respectively. The sea ice volumes calculated for October–November 2005, February–March 2006, October–November 2006, and March–April 2007 were 11,318, 14,075, 10,626, and 13,891 m^3, respectively.

The mission periods of diverse altimetry satellites are limited, making it challenging to estimate the long-term change process of ASI thickness from the observations of a single altimetry satellite. However, combining multi-source and multi-generation satellite altimetry and models can yield long-term, high-precision, and high-resolution ASI thickness data. For example, Kacimi and Kwok [24] combined ICESat-2 and CryoSat-2 to calculate the thickness and volume of ASI from 2018 to 2021.

This study aimed to obtain ASI thickness data with a continuing long-term time series and high spatiotemporal resolution. Overall, the gridded nadirization and sea surface height anomaly methods were used with radar altimetry data from Envisat/CryoSat-2 and laser altimetry data from ICESat-2 to derive ASI freeboard from 2002 to 2021. Combined with the commonplace NASA Eulerian Snow on Sea Ice Model (NESOSIM), the sea ice thicknesses of first-year ice (FYI) and multi-year ice (MYI) were classified and estimated, and the sea ice freeboard and thickness estimations were verified using datasets from Operation IceBridge (OIB), the Climate Change Initiative (CCI), and the Alfred Wegener Institute (AWI). Finally, the influences of surface temperature and surface wind field on sea ice change were also explored.

2. Study Area

The research area in this study is the Arctic Ocean (i.e., north of 66°33′ N), which consists of the Central Arctic and its marginal seas (Beaufort, Chukchi, East Siberian, Laptev, Kara, Barent, and Greenland Seas, and Baffin Bay/Gulf of St. Lawrence, Hudson Bay, and Canadian Arctic Archipelago) (Figure 1). The Arctic Ocean is a nearly closed landlocked sea. It is connected to the Atlantic Ocean through the Greenland and Norwegian Seas and the straits between the Canadian Arctic Archipelago and Baffin Bay, and it is connected to the Pacific Ocean through the Bering Strait.

Figure 1. Study area. Ice type and distribution of altimetry footprints.

3. Data

3.1. Satellite Altimetry Data and Mean Sea Surface (MSS) Model

3.1.1. Envisat Data

Envisat was successfully launched by the European Space Agency (ESA) on 1 March 2002 from the European Spaceport in French Guiana, and the mission ended on 8 April 2012 [25]. Envisat provided continuous oceanic and cryospheric observations covering $\pm 81.5°$ N. Envisat used an advanced Radar Altimeter 2 (RA-2) that emitted a dual-frequency radar signal (Ku-band at 13.575 GHz and S-band at 3.2 GHz) to determine the two-way delay of the radar echo and the power and shape of the radar pulse, allowing it to provide a more accurate sea level. Therefore, in this study, the Envisat Geophysical Data Record (GDR) was used, which includes radar range, orbital altitude, wind speed, wave height, water vapor, and geophysical corrections.

3.1.2. CryoSat-2 Data

CryoSat-2 is a radar altimetry satellite dedicated to polar observation that was successfully launched by the ESA on 8 April 2010 at the Baikonur Cosmodrome in Kazakhstan [26]. CryoSat-2 had an orbital inclination of approximately 92°, orbital height of 717 km, and horizontal space footprint of 250 m. Its repetition period was 369 days, with a sub-cycle period of 30 days. CryoSat-2 covers 88° north–south latitude and has a vertical accuracy of 2.6 cm, providing full Arctic coverage in one month. CryoSat-2 was equipped with a Ku-band synthetic aperture radar mode (SAR)/Interferometric Radar Altimeter (SIRAL), which meets the measurement requirements for ice sheets and sea ice. SIRAL has three measurement modes, that is, low-resolution mode (LRM), synthetic aperture radar mode (SAR), and synthetic aperture radar interference mode (SARIn). For our study, we used level 2 Baseline-D GDR data, which combine these three modalities.

3.1.3. ICESat-2 Data

ICESat-2 was a follow-up mission of ICESat that was successfully launched on 15 September 2018, and it is equipped with an advanced topographic laser altimeter system (ATLAS) [27], a space-borne photon detector. Based on the satellite motion speed, satellite operating height, and pointing angle of the laser transmitter, the diameter of the ATLAS photon footprint is approximately 17 m. The ATLAS instrument measures the time it takes for photons to travel from the ATLAS system to the Earth and back. Combined with the precise positioning of the ATLAS satellite, the latitude, longitude, and elevation of the unique footprint photons in reference to the World Geodetic System 1984 (WGS-84) reference ellipsoid can be determined. Unlike the single-waveform beam of ICESat, ATLAS emits three pairs of laser beams with a wavelength of 532 nm. Each laser beam pair was separated from the emitted laser pulses by diffractive optical elements such that each pair of beams consisted of a strong and a weak beam with an emission energy ratio of 4:1. This 4:1 emission method can provide information with different surface reflectances for the observed objects, which can be used to measure the slope of the objects, thereby improving the accuracy of the ATLAS. Each pair of beams is composed of strong and weak beams, and each pair is separated by 3.3 km across-track. The distance between the strong and weak beams in each pair was approximately 90 m along the cross-track and approximately 2.5 km along the along-track. Here, we adopted the ATL07 dataset, which includes statistics such as surface elevation and type. The main parameters of the three satellites are listed in Table 1 and shown in Figure 2.

3.1.4. MSS Model

The MSS is the displacement of the sea surface relative to a mathematical model of the Earth, and it closely follows the geoid. Before calculating the sea ice freeboard, the MSS height must be removed because of the height measurement bias caused by the geoid. Here, we used the CLS01 MSS provided by Envisat and a series of MSS models, such as DTU15, DTU18, and DTU21 (ftp.space.dtu.dk accessed on 1 May 2022), released by

the Technical University of Denmark (DTU). DTU21 [28] is the latest MSS model, which includes five-year Sentinel-3A and ten-year CryoSat-2 data with three measurement modes. We compared four different MSS models: CLS01, DTU15, DTU18, and DTU21, the details of which are listed in Table 1.
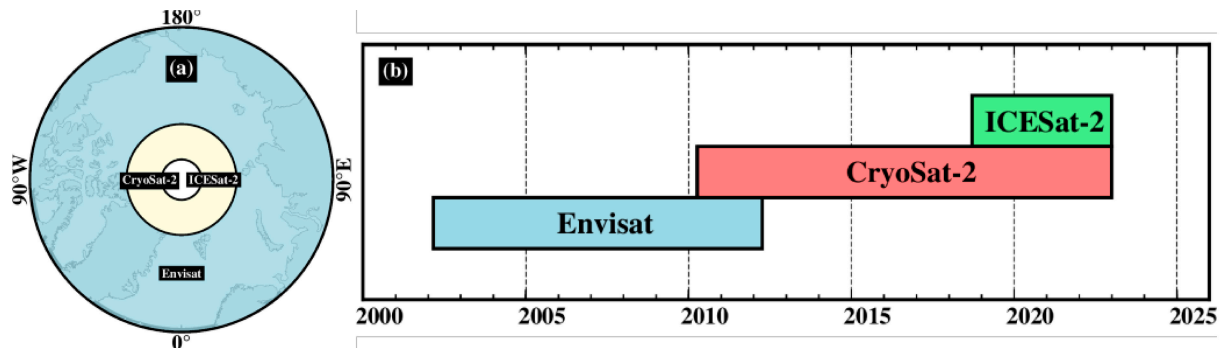

Figure 2. (**a**) Three altimetry satellites' (Envisat, CryoSat-2, and ICESat-2) coverage and (**b**) operating time. Light blue is the maximum spatial extent of Envisat (<81.5° N), and light yellow is the maximum spatial extent of CryoSat-2 and ICESat-2 (<88.0° N).

Table 1. Dataset used in this paper.

| Data Types | Data Source | Spatial Resolution | | Period | Coverage | Orbit Inclination | Reference Ellipsoid | Used |
		Spatial	Time					
Satellite Altimetry	Envisat	ESA (GDR)	—	35 d	2002–2010	81.5° S–81.5° N	98.5°	WGS84	Freeboard retrieval
	CryoSat-2	ESA (GDR)	—	30 d	2010-present	88° S–88° N	92°	WGS84	Freeboard retrieval
	ICESat-2	NASA	—	91 d	2018-present	88° S–88° N	92°	WGS84	Freeboard retrieval
Mean Sea Surface Height	CLS01	Envisat	$2' \times 2'$	—	1993–1999	80° S–82° N	—	Topex/Poseidon	Freeboard retrieval
	DTU15	DTU	$1' \times 1'$	—	1991–2015	90° S–90° N	—	Topex/Poseidon	Freeboard retrieval
	DTU18	DTU	$1' \times 1'$	—	1993–2017	90° S–90° N	—	Topex/Poseidon	Freeboard retrieval
	DTU21	DTU	$1' \times 1'$	—	1993–2020	90° S–90° N	—	Topex/Poseidon	Freeboard retrieval
Ancillary Data	Sea ice type	OSI SAF	10 km	Daily	2005/03-present	Arctic/Antarctic	—	—	Thickness retrieval
	Snow depth	NASA	100 km	Daily	2000–2015	Arctic	—	—	Thickness retrieval
	Snow density	NASA	100 km	Daily	2000–2015	Arctic	—	—	Thickness retrieval
	Sea ice density	Alexandrov (2010)			MYI: 882.0 kg/m^3 FYI: 916.7 kg/m^3				Thickness retrieval
	Sea water density	Alexandrov (2010)			Fixed value: 1024 kg/m^3				Thickness retrieval
	Sea ice area	NSIDC	—	Monthly	1978-present	Arctic	—	—	Volume retrieval
	Sea surface temperature	NOAA	25 km	Daily	1981-present	90° S–90° N	—	—	Impact factors
	Sea surface wind filed	NOAA	varying	Monthly	1948-present	90° S–90° N	—	—	Impact factors

Note: The National Oceanic and Atmospheric Administration (NOAA), European Space Agency (ESA), Technical University of Denmark (DTU), National Snow and Ice Center (NSIDC), first-year ice (FYI), multi-year ice (MYI), and NASA Eulerian Snow on Sea Ice Model (NESOSIM).

3.2. Validation Data

The ESA CCI products [29], AWI sea ice [30], and IceBridge L4 datasets were used to evaluate the accuracy of sea ice thickness in this study. The CCI product was the ASI freeboard and its thickness on a 25 km grid from October 2002 to March 2012. The period of the AWI data was from 2010 to the present. The IceBridge L4 data were a sea ice freeboard measured using an airborne radar.

3.3. Ancillary Data

Sea ice type. Sea ice type is one of the key parameters for determining sea ice thickness. The sea ice type used in this study was issued by the Ocean and Sea Ice Satellite Application Center (OSI SAF) [31], which classifies sea ice into FYI and MYI. The spatial resolution was 10 km, and the period was from March 2005 to the present (ftp://osisaf.met.no accessed on 10 April 2023).

Snow depth. The snow cover product W99 [32], which is widely used in satellite altimetry to estimate sea ice thickness [18,23], has a relatively high degree of accuracy; nevertheless, it can only reflect seasonal changes, and the data are primarily concentrated in the central Arctic. Therefore, the fitting effect of snow depth on the FYI surface area was poor, and the actual snow depth was overestimated. Estimating snow depth using passive microwave radiometers is susceptible to snow humidity and particle size and tends to underestimate the actual snow depth [33,34]. Furthermore, because the microwave signature of snow cover is very similar to that of MYI, the snow depth of MYI cannot be determined precisely [35]. NESOSIM is an open-source snow budget model [36], and the sea ice thickness retrieved by the NESOSIM version 1.0 snow depth was used in this study. The study period was 2000–2015, but the data were only available for winter with a spatial resolution of 100 km.

Snow density. The W99 data confirmed that the average snow density of the Arctic Ocean in September was 250 kg/m^3; however, with the fall and winter snow deposition and accumulation under the action of wind, morphological/density changes in snowpack itself as snowflakes are broken down by mechanical processes, such as saltation, rolling, and blowing snow, the snow density in May also increased to 320 kg/m^3, and the highest density was that of residual snowmelt in July. Alexandrov et al. [37] studied the snow density of Sever Expeditions and found that the average snow density on the FYI from March to May was 324 $\pm$ 50 kg/m^3, which was consistent with the snow density on W99 ice during the same period. Farrell et al. [38] used the IceBridge campaign to obtain a snow depth of 264 kg/m^3 on sea ice in the northern Greenland Sea in April. Therefore, we also used the snow density provided by NESOSIM version 1.0 to estimate ASI thickness.

Sea ice density. Sea ice density is closely related to pure sea ice, brine content, bubbles, and sea ice temperature. It increases with an increase in brine or a decrease in bubbles, which are also closely related to the sea ice type [39]. Alexandrov et al. [37] recalculated the ASI density and its uncertainty based on the Sever Expeditions and concluded that the FYI and MYI densities were quite different, at 916.7 $\pm$ 35.7 kg/m^3 and 882 $\pm$ 23 kg/m^3, respectively. These values have been widely used to determine sea ice thickness. In this study, these densities were adopted as 916.7 kg/m^3 and 882.0 kg/m^3 to calculate the sea ice thickness.

Seawater density. Seawater density was determined based on temperature, salinity, and pressure. Water was incompressible, and pressure had a minimal effect on density, except at extreme depths. This makes temperature and salinity the main determinants of density, with temperature having the greatest impact on density, that is, the lower the temperature, the greater the density. Kwok and Cunningham [23] used 1024 kg/m^3 as the average seawater density and concluded that the seawater density had less uncertainty than the other parameters; therefore, the seawater density in this study was set as 1024 kg/m^3.

Sea ice area. The sea ice area is obtained by multiplying the sea ice extent by the sea ice concentration of the corresponding grid. The sea ice volume was determined by the sea

ice area and thickness. We used the sea ice area provided by the National Snow and Ice Center (NSIDC) from November 1978 to the present.

Sea surface temperature (SST) and sea surface wind field. The emergence and disappearance of ice floes in the Arctic are highly correlated with sea–air interaction and high-latitude weather and climate [40]. Sea ice has strong effects on oceanic and atmospheric dynamics and thermodynamics, which affects sea ice on seasonal, interannual, and even longer time scales. The Arctic temperature is mainly controlled by the North Atlantic Oscillation (NAO) and Arctic Oscillation (AO) [41,42]. Therefore, we took SST and sea surface wind field as the main research objects to explore their influence on sea ice. SST data were obtained from the National Oceanic and Atmospheric Administration (NOAA), and offshore surface wind data were obtained from the National Centers for Environmental Prediction/National Center for Atmospheric Research (NCEP/NCAR) reanalysis data [43]. The detailed data parameters are listed in Table 1.

4. Methodology

First, we used Envisat, CryoSat-2, and ICESat-2 satellite altimetry data to obtain the sea ice region by surface type attribution. Then, the sea ice freeboard was calculated using the gridded nadirization method and the sea surface height anomaly method using the Envisat data. Based on this, the applicability of these two methods was evaluated. Second, the hydrostatic equilibrium equation was used to estimate FYI and MYI sea ice thicknesses. The sea ice volume was then calculated based on the sea ice area. Finally, we analyzed the impact of SST and surface wind fields on sea ice change. The detailed technical process is shown in Figure 3.

4.1. Preprocessing of Altimetry Data

Here, we first performed geophysical corrections on the Envisat GDR and CryoSat-2 GDR products, including inverse pressure, sea state deviation, ionosphere, dry/wet troposphere, and ocean/polar/solid tide corrections [44], and center of gravity offset (OCOG) waveform retracking algorithm [45]. The ICESat-2 products were corrected according to the algorithmic theoretical basis document [46]. Finally, the corrected data were removed according to the three-sigma rule [47].

4.2. Sea Ice Freeboard Inversion Method

The basic principle of satellite altimetry is to use a space-borne microwave/lidar altimeter to determine the height of the satellite to the sub-satellite point on the sea surface by measuring the time elapsed for the microwave/laser to be reflected from the satellite to the ocean surface of the Earth and then back. The sea ice freeboard is the difference between the height of the sea ice surface and the water in open leads, which is the height difference between the floating ice surface and the instantaneous sea surface height. The key to calculating the sea ice freeboard is to obtain high-precision sea ice surface height and instantaneous sea surface height (Figure 4).

The gridded nadirization (25 km longitude × latitude) and sea surface height anomaly methods were used to determine the ASI freeboard from Envisat data. In the gridded nadirization method, the height difference of the nadirization in the grid is considered as the sea surface height, and the difference between the sea ice surface height and the sea surface height is the freeboard. The sea surface height anomaly method was used to determine the freeboard based on the relationship between the sea ice surface height and instantaneous sea surface height. The detailed method is as follows.
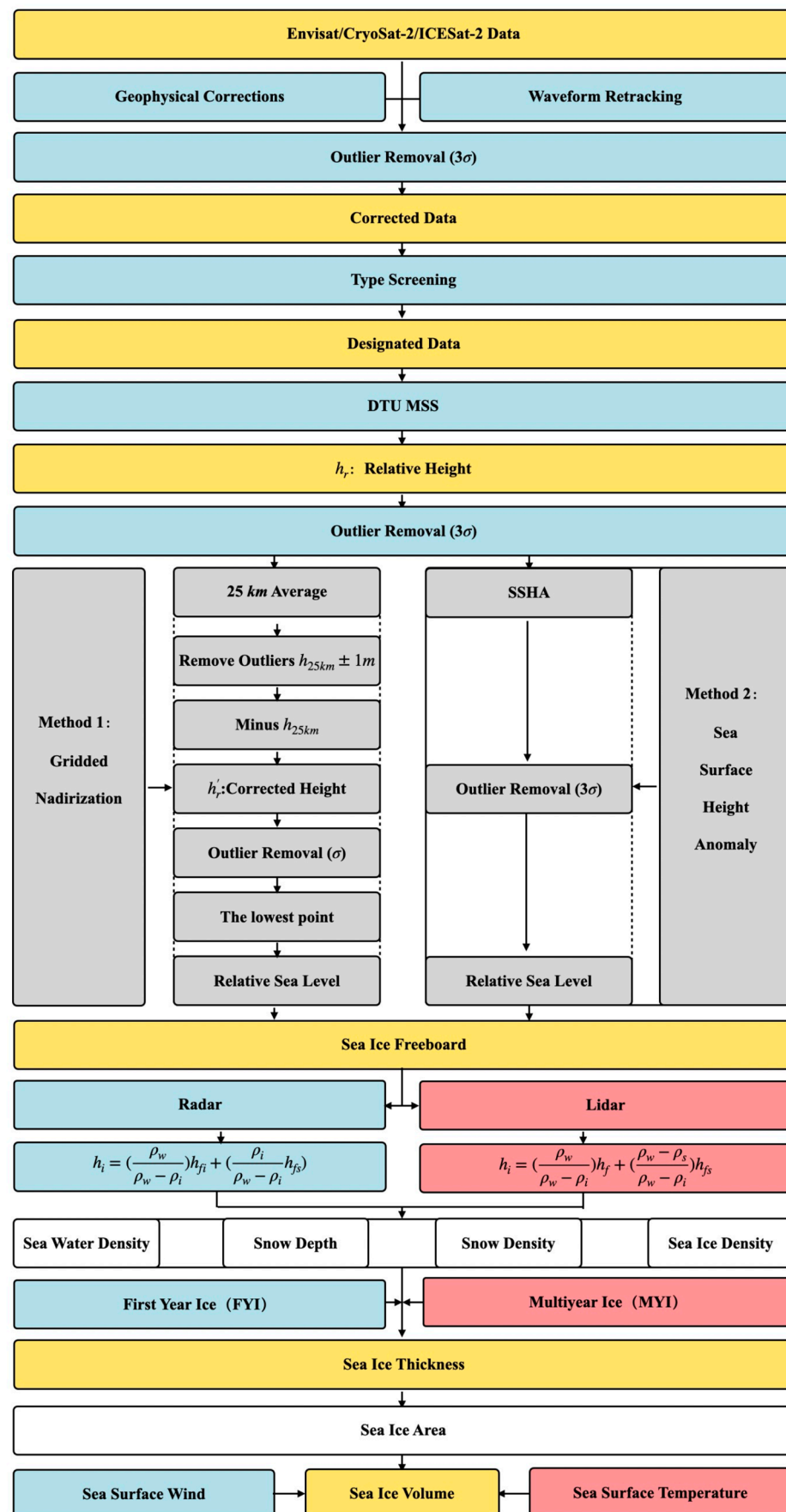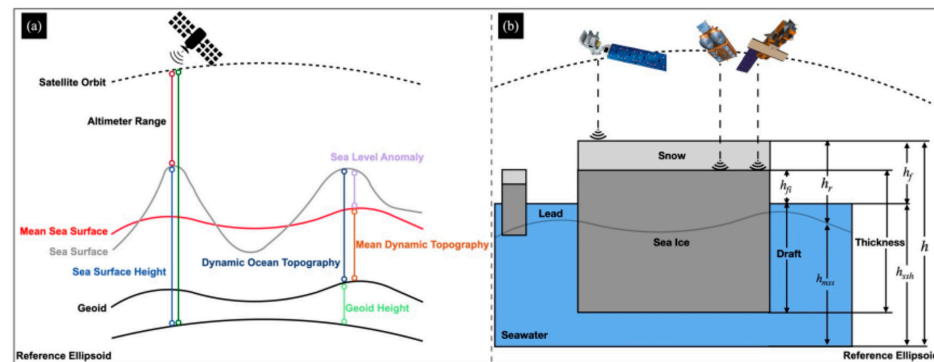
Figure 3. The calculation process of this study.

Figure 4. (**a**) Schematic diagram of satellite altimetry measurement and (**b**) satellite altimetry to determine sea ice freeboard.

4.2.1. The Gridded Nadirization Method

The sea ice freeboard can be determined according to the height difference between the sea ice surface and the local sea surface, as follows:

$$h_f = h - h_{ssh} \tag{1}$$

where h_f is the sea ice freeboard (including snow), h is the distance from the sea ice surface to the reference ellipsoid, and h_{ssh} is sea surface height (Figure 4).

First, geoid fluctuations were removed using the MSS height [48], as follows:

$$h_r = h - h_{mss} \tag{2}$$

Kwok et al. [49] found that the residual error of surface elevation greatly exceeded the expected amplitude of sea ice freeboard when using ICESat to invert the ASI freeboard. Therefore, this study used the average value of the 25 km grid to remove the residual error and obtain the corrected relative elevation, as follows:

$$h_r' = h_r - h_{25km} \tag{3}$$

where h_{25km} was the mean of the 25 km grid of h_r.

Leads can be considered sea level [50], by averaging the elevations of the three lowest points within a 25 km grid and considering this average elevation as the sea surface height (h_{mss}). Finally, the sea ice freeboard can be determined as follows:

$$h_f = h_r' - h_{ssh} \tag{4}$$

4.2.2. Sea Surface Height Anomaly Method

The sea surface height anomaly method was required to obtain high-precision sea ice surface height, and then we used the retracking algorithm to correct it and added various distance corrections. The data were normally obtained by interpolation of observation points in adjacent ice-free sea areas since the instantaneous sea surface height was not measurable under the ice surface. The instantaneous sea surface height was obtained by interpolating the corresponding MSS and sea surface height anomalies of adjacent points. Here, the sea surface height anomaly refers to the difference between the instantaneous sea surface and MSS heights, that is, using the method of interpolating the sea surface height to obtain the instantaneous sea surface height of the sub-satellite point.

The sea ice surface height is calculated as follows:

$$h = h_{sat} - R_{win} - R_{err} - \Delta R \tag{5}$$

where h_{sat} indicates the satellite orbit height, R_{win} and is the window delay correction. The sum of various correction terms related to path propagation delay and geophysical correc-

tions was R_{err}, including dry and wet tropospheric delay, ionospheric delay, sea state bias, ocean tide, solid tide, polar tide, and atmospheric inverse pressure corrections. ΔR is used for OCOG waveform recalculation. The distance is corrected using a tracking algorithm.

The instantaneous sea surface high availability was calculated as follows:

$$h_{ssh} = h_{mss} + SSHA \tag{6}$$

where h_{mss} refers to the MSS height, and $SSHA$ is the sea surface height anomaly. Therefore, the sea ice freeboard is as follows:

$$h_f = h - (h_{mss} + SSHA) \tag{7}$$

4.3. Sea Ice Thickness Inversion Method

Based on the hydrostatic equilibrium equation [37], the sea ice thickness can be estimated by combining the sea ice freeboard with other auxiliary data. For radar altimetry satellites, previous studies have shown [51] that in cold and dry conditions, Ku-band electromagnetic waves can almost pass through the ice–snow interface, as follows:

$$h_i = \left(\frac{\rho_w}{\rho_w - \rho_i} \right) h_{fi} + \left(\frac{\rho_i}{\rho_w - \rho_i} h_{fs} \right) \tag{8}$$

and for laser altimetry satellites, as follows:

$$h_i = \left(\frac{\rho_w}{\rho_w - \rho_i} \right) h_f + \left(\frac{\rho_w - \rho_s}{\rho_w - \rho_i} \right) h_{fs} \tag{9}$$

where h_{fi} was the sea ice freeboard determined by the radar altimeter, h_f was the sea ice freeboard measured by the laser altimeter, ρ_w was the seawater density (1024 kg·m^{-3}), h_{fs} and ρ_s were the snow depth and snow density that vary with time and space, respectively, and ρ_i was sea ice density (FYI: 916.7 kg·m^{-3}, MYI: 882.0 kg·m^{-3}).

To address spatial resolution differences between NESOSIM and Envisat, CryoSat-2, and ICESat-2, we interpolated the 100 km resolution snow depth to 25 km. Additionally, the time span of NESOSIM was 2000–2015; therefore, we took the monthly average from this timeframe as the snow depth and sea ice type (i.e., FYI and MYI) provided by the Ocean and Sea Ice Satellite Application Facility (OSI SAF) into the hydrostatic equilibrium equation to determine the sea ice thickness.

4.4. Inversion of Sea Ice Volume

The sea ice volume in a grid cell is the product of the average cell sea ice thickness and the cell area. The Arctic Ocean's sea ice volume is the sum of the volumes of all grid cells covered by sea ice. For simplicity, the product of the sea ice area and annual mean thickness is defined as the total volume of sea ice in the Arctic Ocean, as follows:

$$V = \Sigma(h_i \times S) \tag{10}$$

where h_i is the sea ice thickness, and S is the sea ice area (described in Section 3.3).

5. Results and Discussion

5.1. Validation and Evaluation of the MSS Height Model

To effectively remove the undulations caused by the geoid and sea surface topography, the sea ice freeboard and sea ice thickness should be accurately determined. Here, we compared the four MSS height models, that is, CLS01, DTU15, DTU18, and DTU21, and based on the same survey line (Figure 5 and Table 2), the Frechet distance method [52] was used to judge the similarity between the satellite surface elevation and MSS height. This method was based on two-directional curves that could not be backtracked, and the

shortest maximum distances between these curves were computed. Therefore, the smaller the calculated result, the better it fits with the curves.
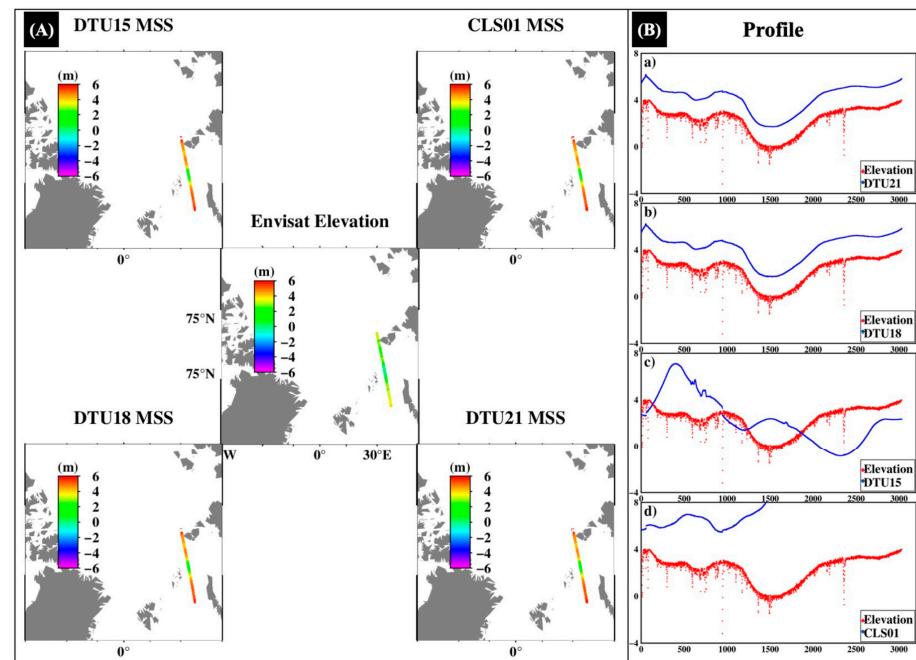

Figure 5. (**A**): Envisat and four MSS models on the same survey line sea surface height; (**B**): (a–d) the red dots represent the WGS84 elevation, and the blue dots represent the CLS01, DTU15, DTU18, and DTU21 MSS.

Table 2. The results of the similarity comparison between the Envisat surface elevation and the MSS model.

MSS Model	Level of Dissimilarity
CLS01	7.8639
DTU15	7.9878
DTU18	12.0550
DTU21	2.9542×10^3

Note: the Technical University of Denmark (DTU).

The lower resolution caused the relative heights of CLS01 to retain residuals of geoid fluctuations in regions with large MSS fluctuations, while the relative heights of DTU15 and DTU18 were much smoother, implying that both MSS models were sufficient at removing geoid undulations. The relative heights displayed by the DTU15 and DTU18 showed subtle differences; however, compared to DTU15 and DTU18, DTU21 contained more satellite observation data and a longer time series. Therefore, we adopted the DTU21 model for our calculations.

In the gridded nadirization method, to ensure the integrity of valid data and eliminate elevation outliers, we first calculated the standard deviation (SD) of the hr' of each 25 km grid of Envisat. Elevation values exceeding h25 km $\pm N$ SD were considered outliers according to the error-handling criteria. Furthermore, h25 km was the mean value within the 25 km grid, and N was a multiple of the SD. Table 3 details that when $N = 0.5$, a large amount of data was excluded, including some useful information, while for $N = 3$ or $N = 2$, the rejection rate was too low, still allowing for outliers. When $N = 1$, the elevation distribution was at a reasonable level, and the integrity of the data was maintained; therefore, we selected $N = 1$.

Table 3. Rejection rate of different multiple standard deviations.

Grid	N = 3			N = 2			N = 1			N = 0.5	
	Total Number of Original Points	Total Number after Filtered Points	Rejection Rate (%)	Total Number of Filtered Points	Rejection Rate (%)	Total Number after Filtered Points	Rejection Rate (%)	Total Number after Filtered Points	Rejection Rate (%)
Sample1	16,476	15,888	3.56	15,249	7.45	11,802	28.37	6717	59.23
Sample2	16,965	16,431	3.14	15,714	7.34	12,363	27.13	6927	59.17
Sample3	15,302	14,738	3.68	14,328	6.37	12,187	20.36	6950	54.58
Sample4	16,353	15,678	4.12	15,135	7.45	12,012	26.55	6345	61.20
Sample5	16,806	16,008	4.74	15,480	7.89	11,997	25.43	6636	60.51

5.2. Calculation of ASI Freeboard Using Envisat/CryoSat-2/ICESat-2

5.2.1. Using Envisat to Calculate Sea Ice Freeboard

The summer sea ice surface-melt ponds bring great uncertainty to determining sea ice freeboard [53]. Therefore, this study only estimated the sea ice freeboard from October to April of the following year (i.e., the sea ice freezing season) [54]. Here, the gridded nadirization (M1) and sea surface height anomaly (M2) methods were used to calculate the ASI freeboard from October 2002 to April 2012 based on Envisat altimetry data (Figure 6a). Figure 7A shows the spatial distribution of ASI freeboard during the freeze-up period using the gridded nadirization method based on Envisat altimetry data. The sea ice grows rapidly, with its coverage extending to the Beaufort, Chukchi, and East Siberian Seas. This increase in freeboard was not significant compared to the change in range. From February to April, the freeboard in the central Arctic exhibited a clear upward trend in height. Except for the change in freeboard coverage, there was no significant change in the coverage of the Greenland Sea.

These results showed that the average value of the ASI freeboard was the smallest in October every year, and along with the continuous decrease in Arctic Ocean temperature, the sea ice freeboard began to increase. In December and January of the following year, the sea ice continued to grow and reached its maximum in April. Second, the maximum sea ice freeboard was mostly concentrated near the Canadian Arctic Islands, and with the expansion of the sea ice extent in November, it rapidly expanded to the East Siberian and Barents Seas.

It can be seen from Table 4 and Figure 6a that the gridded nadirization method was better than the sea surface height anomaly method. Therefore, this study only adopted the gridded nadirization method for freeboards in the subsequent calculations of CryoSat-2 and ICESat-2. The ASI thickness was then determined.

Table 4. Mean bias error, root-mean-square error (RMSE), and standard deviation (STD).

| Month | CCI | | | | | |
	Gridded Nadirization			SSHA		
October	Bias/m	RMSE/m	STD/m	Bias/m	RMSE/m	STD/m
November	0.12	0.15	0.09	0.25	0.30	0.29
December	0.12	0.14	0.08	0.25	0.30	0.28
January	0.11	0.14	0.08	0.24	0.28	0.28
February	0.11	0.13	0.08	0.24	0.28	0.27
March	0.09	0.13	0.09	0.18	0.20	0.27
April	0.10	0.14	0.10	0.19	0.21	0.28
Overall	0.11	0.14	0.09	0.22	0.22	0.28

5.2.2. Calculation of Sea Ice Freeboard Using CryoSat-2

Figure 6a shows that the freeboard retrieved by CryoSat-2 was in good agreement with Envisat, and most of the freeboards were 0.2 m. Additionally, we used the IceBridge mission in March 2011 to verify the sea ice freeboard determined using CryoSat-2. Figure 7B shows the spatial distribution of ASI freeboards in the congelation season based on CryoSat-2. The distribution of the freeboard of CryoSat-2 was approximately similar to that of Envisat. Envisat observes thicker ice in the marginal seas than CryoSat-2. Owing to the higher orbital inclination of CryoSat-2, it covers a wider area of the Arctic; therefore, it shows more clearly that the sea ice has grown rapidly in the direction of the Bering Strait since October. The coverage of sea ice has not changed significantly since February, but the freeboard of the MYI in central Arctic waters has increased significantly.

Figure 8a shows that most of the Operation IceBridge flight routes are in the Canadian Arctic Archipelago and northern Greenland, where the sea ice is thicker, and the detection of thin ice is more difficult than that of thicker sea ice. Therefore, using the data for comparison is more effective. Here, we used bi-linear to interpolate the CryoSat-2 sea ice freeboard to the corresponding observation points of the Operation IceBridge, and the

difference between the satellite freeboard and the IceBridge freeboard and its statistical results were calculated. The spatial distribution is shown in Figure 8b,c. The results show that 53,378 points were consistent with the freeboard of the IceBridge campaign, and the freeboard measured by 53,418 satellite observations was 0.2 m lower than the observation value of the IceBridge.
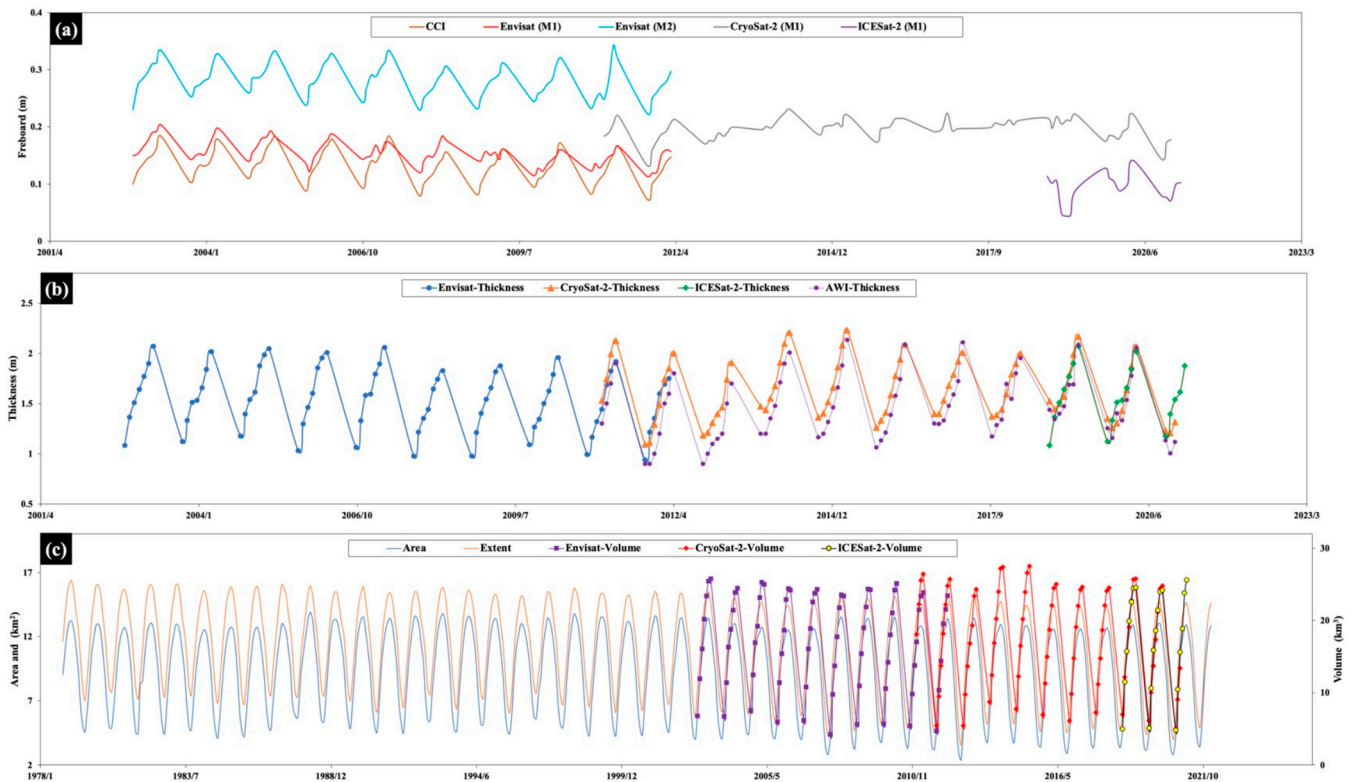

Figure 6. Sea ice (**a**) freeboard, (**b**) thickness, (**c**) area, extent, and volume changes. Note: sea ice freeboard and thickness are only observed in one congelation season (October to April) value.

5.2.3. Using ICESat-2 to Calculate Sea Ice Freeboard

The spatial distribution of ICESat-2 freeboard inversion using the gridded nadirization method (Figure 7C) showed that because the ICESat-2 data had only 18 d in October 2018, the points in space were sparser than those in other months. Figure 7 shows that the spatial distribution of the freeboard of ICESat-2 was the same as that of CryoSat-2 and Envisat. From October each year, sea ice began to spread rapidly into the East Siberian, Laptev, and Kara Seas. The areas with high freeboard were concentrated in the Canadian Arctic Archipelago, where ice has existed for many years, and the central Arctic Ocean in northern Greenland and Svalbard; however, the freeboard distribution of ICESat-2 was more obvious than those of Envisat and CryoSat-2. The freeboard in the Chukchi Sea started to increase from February each year until it reached its maximum in April.
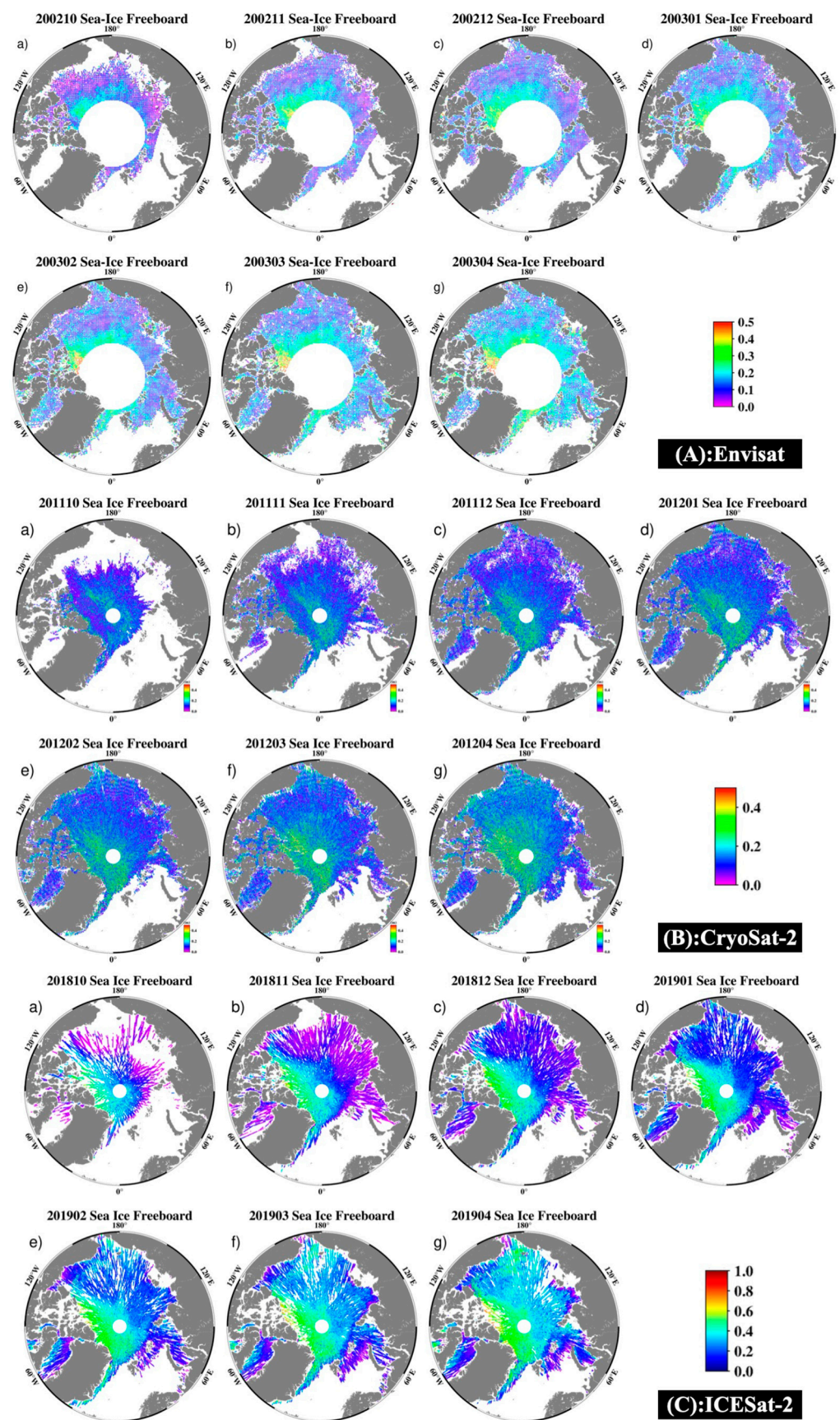
Figure 7. (**A**) Envisat, (**B**) CryoSat-2, and (**C**) ICESat-2 One congelation season. (a–g) Spatial distribution of sea ice freeboard from October to April each year.
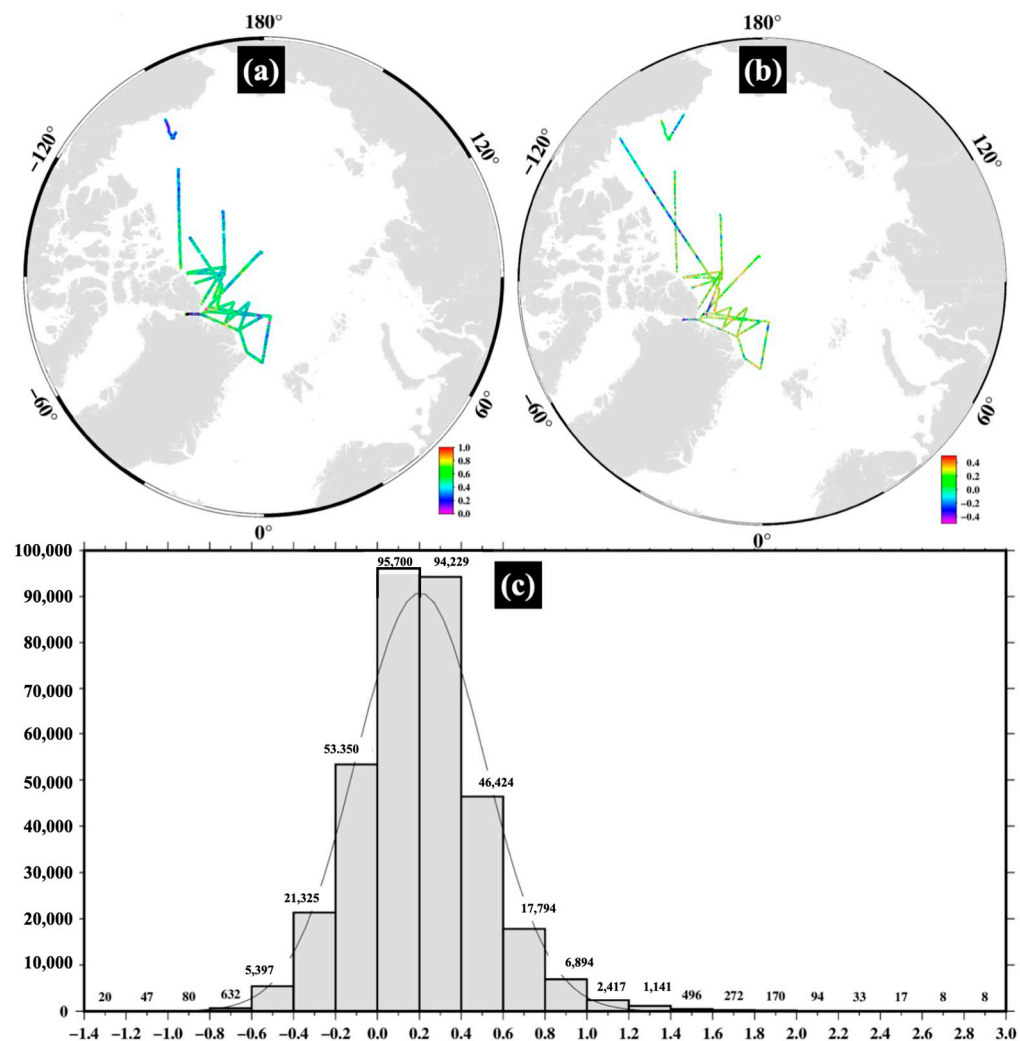
Figure 8. (**a**) IceBridge freeboard in March 2011; (**b**) differences between CryoSat-2 freeboard and IceBridge freeboard; and (**c**) the statistical differences.

5.3. Sea Ice Thickness

Figure 6a shows that the sea ice freeboard determined by the CCI, M1, and M2 methods based on Envisat, CryoSat-2, and ICESat-2 data had good seasonal agreement; however, there were amplitude differences. The sea ice freeboard determined by the M1 method, based on Envisat data, was more consistent with the CryoSat-2 results. The amplitude differences in these observations were primarily due to snow depth inconsistencies, where satellite radar can penetrate snow, and the determining sea ice freeboard includes snow changes and is therefore significantly higher than the sea ice determined by laser altimetry onboard ICESat-2. However, when using the hydrostatic equilibrium equation to determine sea ice thickness, snow thickness's influence was considered. Therefore, the ASI thickness determined based on Envisat, CryoSat-2, and ICESat-2 data had a very high degree of accuracy in both seasonal and amplitude terms. The correlation coefficient between CryoSat-2 and AWI reached 0.95, showing good agreement and consistency with the AWI results (Figure 6b).

Figure 6b shows that the thickness of sea ice was the thinnest in October every year, and the increase in sea ice freeboard and thickness of sea ice increased until they reached their maximum values in April of the winter-season data. Moreover, the average sea ice thickness within the Arctic Circle is between 0.5 and 2.5 m. Sea ice thickness estimated from Envisat data had a rate of -0.15 ± 0.09 cm/year during 2002–2012 and -0.11 ± 0.07 cm/year during 2010–2021 based on sea ice thickness estimated from CryoSat-2 observations, and

sea ice thickness estimated by ICESat-2 observations had a rate of -0.19 ± 0.03 cm/year during 2018–2021 and -0.13 ± 0.02 cm/year during 2002–2021.

Figure 9 shows the spatial distribution of the FYI and MYI in October, November, and December 2005 and January, February, March, and April 2016 (i.e., Arctic winter). The results showed that, during the sea ice freezing season, both the FYI and MYI areas increased; however, in general, the extent of these sea ice types decreased from 2005 to 2021. Sea ice thickness is at a minimum in October, and after the summer melt it is at a maximum in April. The MYI coverage changed relatively gently and is concentrated in the Canadian Arctic Islands, the western side of the central Arctic, and in the Beaufort and Chukchi Seas. The FYI extent expanded rapidly in October to include the Barents, Kara, East Siberian, and Laptev Seas. After April, the temperature rose and gradually melted until October, at the start of the next freezing period.

Figure 9. Spatial distribution of FYI and MYI in winter season.

5.4. Sea Ice Volume

The ASI extent and area (Figure 6c) were multiplied by its thickness (Figure 6b) to estimate the volume. Figure 6c shows that the sea ice extent and area showed a clear downward trend from 2002 to 2021 (approximately 156 km^2/year and 113 km^2/year, respectively). Additionally, the sea ice volume decreased by approximately 5437 km^3 each month. In March each year, the extent and area of Arctic Ocean sea ice were at their maximums, and in September each year, they were at their minimums.

Existing sea ice volume products are relatively lacking; therefore, we compared the sea ice volume with previous studies. Hilmer and Lemke [55] used environmental data to simulate ASI volume for 37 years (1958–1995) in the range of 26,000–34,000 km^3, with October–November having the minimum sea ice volume and March–May having the maximum sea ice volume. Schweiger et al. [56] reconstructed the sea ice volume from 1901 to 2010 using environmental data studies. The sea ice volume in April was primarily within 30,000–40,000 km^3, and in September, the sea ice volume was primarily within 10,000–20,000 km^3. After 2000, the sea ice volume in September began to fall below 10,000 km^3. Furthermore, Kacimi and Kwok [24] used CryoSat-2 and ICESat-2 observations to study the MYI and one-year Arctic sea ice volumes from 2018 to 2021, during which time the overall sea ice volume showed a downward trend, and from October to the following year the MYI volume in April was between 0 and 8000 km^3. The sea ice volumes estimated by the three satellites in this study reached their maximum values in April every year and minimum values in October every year. These sea ice volume values had obvious seasonal changes, and the sea ice volume is between 4000–26,000 km^3. The sea ice volumes derived in this study are generally consistent with those of these previous studies.

5.5. Analysis of Influencing Factors

5.5.1. Sea Surface Temperature

Here, we analyzed temperature variations between 2002 and 2021 (Figure 10). For 20 years, the SST of the Arctic Ocean has increased by 0.003 °C per month. The average SST in the Arctic Circle was the lowest every March, the SST started to rise slowly from April to May, and the SST rose rapidly in June until it reached its maximum in August. Finally, the SST began to plummet in September until the downward trend weakened markedly in December before dropping to its minimum in March of the following year.

Figure 10. Boxplot of monthly average temperature in the Arctic Circle from 2002 to 2021. The blue line represents the monthly average change curve, the red dot represents the monthly median, and the yellow line represents the temperature change trend.

Arctic SST changes have obvious periodicity, and the average monthly SST is greater than the median, indicating that some sea areas are warmer than others. Additionally, the surface temperatures are not normally distributed and are highly skewed, owing to the warm ocean carrying heat across the Atlantic from the Gulf of Mexico to coastal Scandinavia. Combined with the spatial distribution of the monthly mean SST within the Arctic Ocean (Figure 11), the annual temperature in the central Arctic waters, Beaufort Sea, and Canadian Arctic Archipelago is below 0 °C but shows an overall upward trend each year. Additionally, warming trends are evident across most of the Arctic region. The monthly SST in the Barents Sea is the highest of the entire Arctic region, and the radiated SST decreased slowly from the Barents Sea outward. The FYI surface temperature was relatively low, while that in the MYI area was the lowest, and it was highly consistent with the division of sea ice types. In the season when sea ice freeboard and thickness decrease, SST gradually rose from the marginal seas, especially the Barents and Kara Seas on the east side of Svalbard, and in the Fram Strait on the left side of Svalbard. The Chukchi and Baft Seas are prominent in the Bering Strait in the Arctic and Pacific Oceans.

In this study, the correlation between temperature and area and its extent were analyzed (Figure 12), and the correlation between temperature and area was −0.9; however, the extreme SST values did not correspond to those of sea ice freeboard and thickness. Temperature changes preceded the changes in sea ice; therefore, a one-month lag analysis was carried out, and the correlation coefficient between temperature and area was −0.96, which indicated that the response of sea ice peaked one month after the temperature change. Therefore, the SST is one of the most important factors driving changes in sea ice.
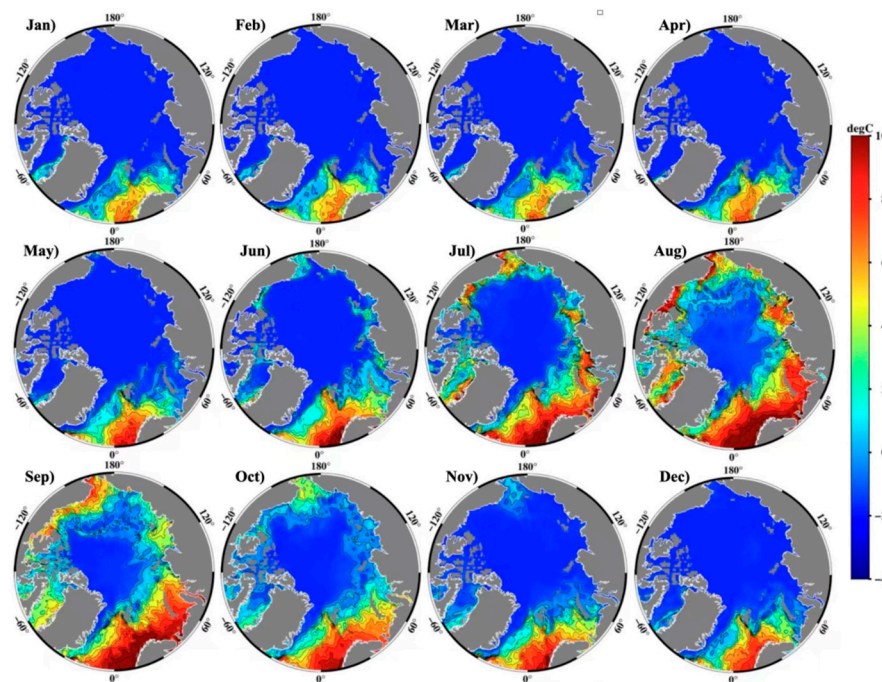
Figure 11. Spatial distribution of monthly mean sea surface temperature in the Arctic Ocean from 2002 to 2021 (January to December).
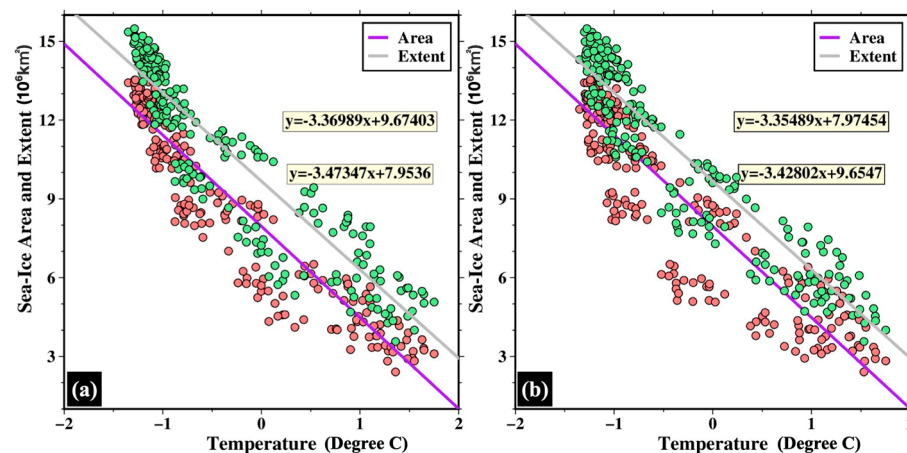

Figure 12. (**a**) Correlation between sea surface temperature and sea ice extent and (**b**) between sea surface temperature and sea ice extent with a one-month lag in sea surface temperature.

Furthermore, the annual offshore surface temperature increased in the summer and decreased in the winter. There was a significant negative correlation between the ASI area and temperature. The spatiotemporal temperature distribution (Figures 10–12) shows that in areas with high temperature, the area and extent of ASI were significantly lower, but the SST was not synchronized with the freeboard, and the thickness of sea ice had a one-month lag.

5.5.2. Surface Wind Field

This study analyzed the monthly average wind field on the Arctic offshore surface from 2002 to 2021 (Figure 13). The results showed that throughout the entire Arctic region, there were no noticeable changes in the wind field, but there were two notable places: one was the divergent anticyclone near the Beaufort Sea, and the other was the transpolar airflow through Nansen-Gakor from Eastern Siberia. The transpolar airflow was most obvious along the eastern coast of Greenland (Figure 14), which blows to the North Atlantic

through the Fram Strait throughout the year. Surrounded by land, sea ice in the Beaufort Gyre collides and accumulates near the Canadian Arctic Islands, and the SST here is lower, so the sea ice has sufficient time to form, forming thicker MYI. Resulting from the transpolar airflow, sea ice is blown away, moved, and broken up by the wind, and the temperature is relatively high, making it difficult for the sea ice to spend a full summer, thus forming FYI. On the east coast of the Greenland Sea, the combined effect of wind and sea temperature causes substantial amounts of sea ice to melt and flow into the North Atlantic along with transpolar airflow. Near-surface winds are a dominant factor in the redistribution of snow on the sea ice surface and drift; however, the seasonal wind direction in the Arctic Circle is approximately the same every year, with distinct seasonal characteristics. Therefore, the sea surface wind field is also an important factor affecting the changes in ASI.
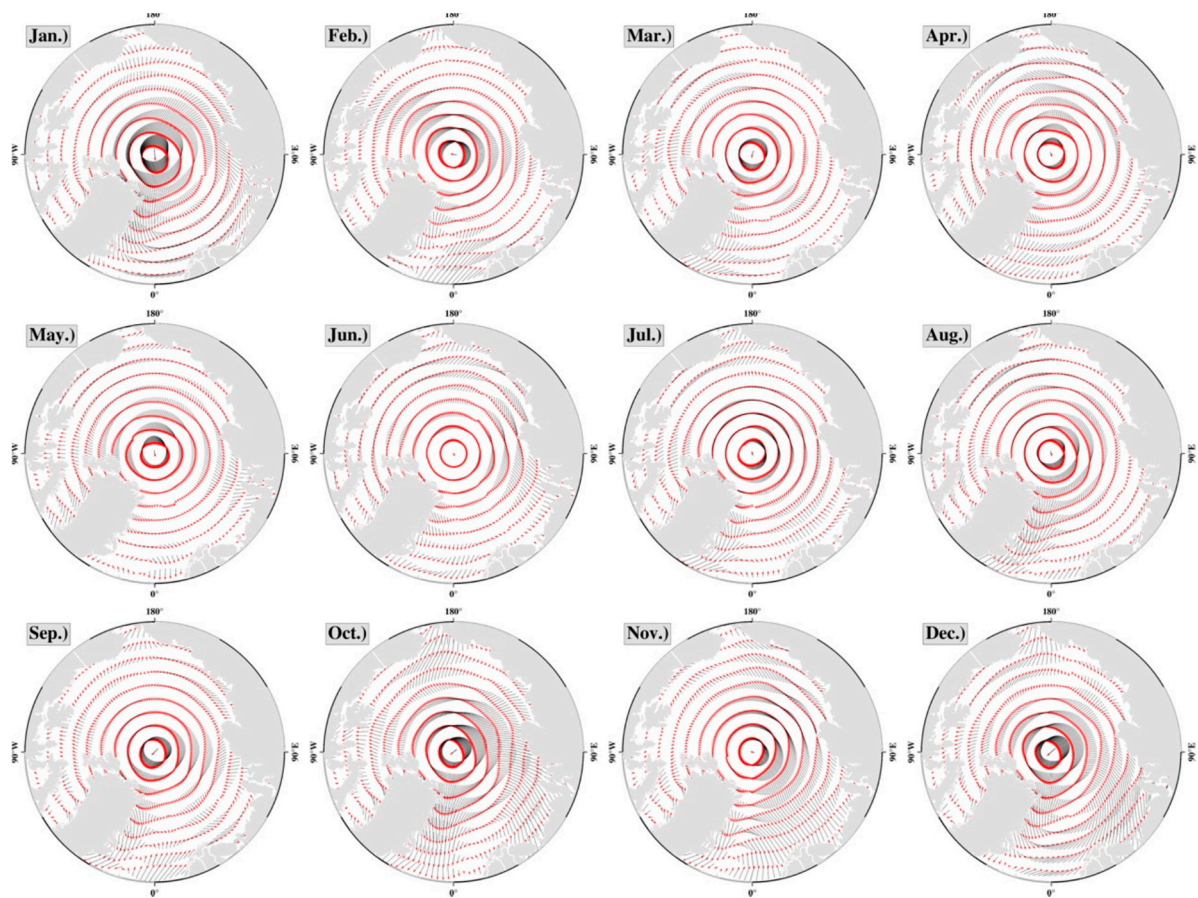

Figure 13. Schematic diagram of the monthly average wind field from 2002 to 2021. The red arrow represents the wind direction, the size of the arrow represents the wind speed, and it represents the average value of the wind field from January to December, respectively.

The Fram Strait between Greenland and Svalbard is the main channel for sea ice loss, with approximately 90% of the sea ice flowing from the Arctic Ocean into the East Greenland Cold Current. Therefore, this area was analyzed as an example. Throughout the year, meridional winds blow from the central Arctic region along the eastern coast of Greenland to the North Atlantic each month, which is highly consistent with the distribution of sea ice freeboard and thickness in the Greenland Sea. Each July, August, and September, the wind speed in this area also gradually increased, and the sea ice flowing into the Atlantic Ocean increased, which further led to the loss of sea ice in the summer. In the winter, the wind speed gradually increased, providing a good wind field environment for the growth of sea ice.
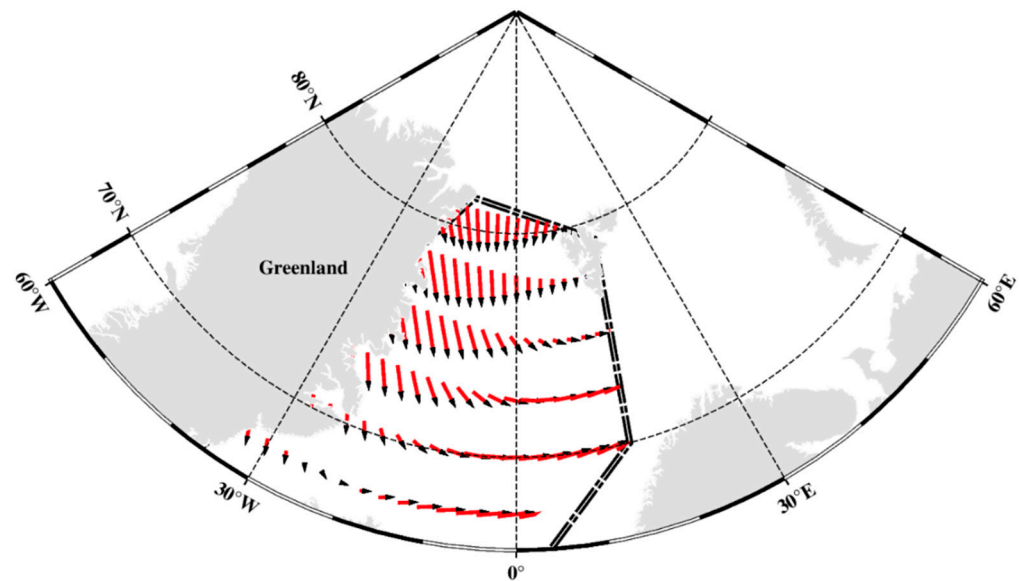
Figure 14. Annual mean wind speed and direction along the eastern coast of Greenland. The length of the arrow is the average wind speed, and the direction of the arrow is the wind direction.

6. Conclusions

In this study, Arctic sea ice (ASI) thickness was obtained from the three altimetry satellite datasets, that is, Envisat, CryoSat-2, and ICESat-2, by combining the hydrostatic equilibrium equation (Equations (8) and (9)). The spatiotemporal evolution of ASI thickness and volume from 2002 to 2021 was verified by comparing data from CCI, Operation IceBridge, and AWI, and the relationship between SST and sea surface wind field and sea ice area, thickness, and volume was obtained. The main conclusions are as follows:

(1) Based on the comparison of the sea ice freeboard and sea ice thickness changes determined by Envisat, CryoSat-2, and ICESat-2 data, external inspection data and existing research results were relatively consistent, indicating that the 2002–2021 sea ice freeboard determined in this study was valid for the thickness results.

(2) ASI freeboard and thickness variations showed obvious seasonal characteristics, that is, in October every year, the ASI freeboard and thickness reached their minimum, after which the sea ice freeboard and thickness gradually increased and reached their maximum in April. Moreover, the maximum value of ASI freeboard and thickness was predominantly concentrated near the Canadian Arctic Islands, and the sea ice extent expanded every November, rapidly expanding to the East Siberian and Barents Seas.

(3) From 2002 to 2021, the rate of change in ASI freeboard and thickness was -0.20 ± 0.04 cm/year and -0.13 ± 0.02 cm/year, respectively; the rate of change in ASI area and extent was 156 km^2/year and 113 km^2/year, respectively, and the volume of sea ice decreased by approximately 5437 km^3 during the winter month. The extent and area of sea ice in the Arctic Ocean reached their maximum each March and their minimum each September.

(4) From 2002 to 2021, the Arctic SST increased by 0.003 °C per month. SST was one of the most important factors driving sea ice changes, but it lagged behind sea ice changes by one month.

(5) The sea surface wind field is also an important factor affecting changes in ASI. The meridional wind blowing from the central Arctic region along the eastern coast of Greenland to the North Atlantic every month is related to the sea ice freeboard and thickness in the Greenland Sea.

In summary, the gridded nadirization method can obtain the sea ice freeboard value more quickly. The regional average sea ice thickness and volume as well as their change rates can be determined based on the gridded nadirization method. The sea ice freeboard, thickness, and volume during the sea ice melt season (May–September) were not estimated

in this study because of the influence of Arctic summer melt ponds and snow cover. Future research should combine multi-source satellite altimetry data to study the sea ice freeboard in the Arctic summer (sea ice melting season) and the effect of melt ponds on sea ice thickness.

Author Contributions: Conceptualization, N.C. and Y.Z.; writing—original draft preparation, Y.Z. and N.C.; writing—review and editing, F.L., L.Y., S.W., G.C., Z.W., N.Y., R.S. and G.O.; All authors have read and agreed to the published version of the manuscript.

Institutional Review Board Statement: Not applicable.

Informed Consent Statement: Not applicable.

Data Availability Statement: Monthly and daily observational data used in this study are publicly available. Envisat data can be found at https://earth.esa.int/eogateway/missions/envisat (accessed on 12 April 2022). CryoSat-2 data are available at http://science-pds.cryosat.esa.int (accessed on 13 April 2022). ICESat-2 data are available at https://icesat-2.gsfc.nasa.gov/science/data-products (accessed on 14 April 2022). DTU MSS are available at ftp.space.dtu.dk (accessed on 1 May 2022). Sea ice type data are available at https://osi-saf.eumetsat.int/products/sea-ice-products (accessed on 2 May 2022). Snow model can be found at https://earth.gsfc.nasa.gov/cryo/data/nasa-eulerian-snow-sea-ice-model-nesosim (accessed on 3 May 2022). Sea ice area and extent data are from https://nsidc.org/data/seaice_index (accessed on 18 June 2022). Sea surface temperature and wind field data are available at https://www.ospo.noaa.gov/Products/ocean (accessed on 19 June 2022). AWI data are available at https://data.meereisportal.de/data/ (accessed on 20 June 2022). CCI data can be found at https://data.ceda.ac.uk/neodc (accessed on 21 June 2022). OIB data are available at https://n5eil01u.ecs.nsidc.org (accessed on 22 June 2022).

Conflicts of Interest: The authors declare no conflict of interest.

References

1. Dai, A.; Luo, D.; Song, M.; Liu, J. Arctic amplification is caused by sea-ice loss under increasing CO2. *Nat. Commun.* **2019**, *10*, 121. [CrossRef] [PubMed]
2. Lin, Y.; Moreno, C.; Marchetti, A.; Ducklow, H.; Schofield, O.; Delage, E.; Meredith, M.; Li, Z.; Eveillard, D.; Chaffron, S.; et al. Decline in plankton diversity and carbon flux with reduced sea ice extent along the Western Antarctic Peninsula. *Nat. Commun.* **2021**, *12*, 4948. [CrossRef] [PubMed]
3. Kwok, R.; Cunningham, G.F.; Wensnahan, M.; Rigor, I.; Zwally, H.J.; Yi, D. Thinning and volume loss of the Arctic Ocean sea ice cover: 2003–2008. *J. Geophys. Res. Oceans* **2009**, *114*, C07005. [CrossRef]
4. Lindsay, R.; Schweiger, A. Arctic sea ice thickness loss determined using subsurface, aircraft, and satellite observations. *Cryosphere* **2015**, *9*, 269–283. [CrossRef]
5. Vaughan, D.G.; Comiso, J.C.; Allison, I.; Carrasco, J.; Kaser, G.; Kwok, R.; Mote, P.; Murray, T.; Paul, F.; Ren, J.; et al. Observations: Cryosphere. In *Climate Change 2013: The Physical Science Basis. Contribution of Working Group I to the Fifth Assessment Report of the Intergovernmental Panel on Climate Change*; Cambridge University Press: Cambridge, UK, 2013.
6. Curry, J.A.; Schramm, J.L.; Ebert, E.E. Sea ice-albedo climate feedback mechanism. *J. Clim.* **1995**, *8*, 240–247. [CrossRef]
7. Sedlar, J.; Tjernström, M.; Mauritsen, T.; Shupe, M.D.; Brooks, I.M.; Persson, P.O.G.; Birch, C.E.; Leck, C.; Sirevaag, A.; Nicolaus, M. A transitioning Arctic surface energy budget: The impacts of solar zenith angle, surface albedo and cloud radiative forcing. *Clim. Dyn.* **2011**, *37*, 1643–1660. [CrossRef]
8. Aagaard, K.; Carmack, E.C. The role of sea ice and other fresh water in the Arctic circulation. *J. Geophys. Res.* **1989**, *94*, 14485–14498. [CrossRef]
9. Serreze, M.C.; Barrett, A.P.; Slater, A.G.; Woodgate, R.A.; Aagaard, K.; Lammers, R.B.; Steele, M.; Moritz, R.; Meredith, M.; Lee, C.M. The large-scale freshwater cycle of the Arctic. *J. Geophys. Res. Oceans* **2006**, *111*, C11010. [CrossRef]
10. Brandon, M.A.; Cottier, F.R.; Nilsen, F. Sea Ice and Oceanography. In *Sea Ice*, 2nd ed.; Blackwell Publishing Ltd.: Hoboken, NJ, USA, 2010. [CrossRef]

11. Regehr, E.V.; Hunter, C.M.; Caswell, H.; Amstrup, S.C.; Stirling, I. Survival and breeding of polar bears in the southern Beaufort Sea in relation to sea ice. *J. Anim. Ecol.* **2010**, *79*, 117–127. [CrossRef] [PubMed]

12. Wadhams, P.; Wilkinson, J.P.; McPhail, S.D. A new view of the underside of Arctic sea ice. *Geophys. Res. Lett.* **2006**, *33*, L04501. [CrossRef]

13. Djepa, V. Improved Retrieval of Sea Ice Thickness and Density from Laser Altimeter. *Atmos. Clim. Sci.* **2014**, *4*, 907–918. [CrossRef]

14. Kwok, R. Satellite remote sensing of sea-ice thickness and kinematics: A review. *J. Glaciol.* **2011**, *56*, 1129–1140. [CrossRef]

15. Francis, J.A.; Vavrus, S.J. Evidence linking Arctic amplification to extreme weather in mid-latitudes. *Geophys. Res. Lett.* **2012**, *39*, L06801. [CrossRef]

16. Schweiger, O.; Settele, J.; Kudrna, O.; Klotz, S.; Kühn, I. Climate change can cause spatial mismatch of trophically interacting species. *Ecology* **2008**, *89*, 3472–3479. [CrossRef]

17. Singarayer, J.S.; Bamber, J.L.; Valdes, P.J. Twenty-first-century climate impacts from a declining Arctic sea ice cover. *J. Clim.* **2006**, *19*, 1109–1125. [CrossRef]

18. Laxon, S.; Peacock, H.; Smith, D. High interannual variability of sea ice thickness in the Arctic region. *Nature* **2003**, *425*, 947–950. [CrossRef] [PubMed]

19. Giles, K.A.; Laxon, S.W.; Ridout, A.L. Circumpolar thinning of Arctic sea ice following the 2007 record ice extent minimum. *Geophys. Res. Lett.* **2008**, *35*, L22502. [CrossRef]

20. Laxon, S.W.; Giles, K.A.; Ridout, A.L.; Wingham, D.J.; Willatt, R.; Cullen, R.; Kwok, R.; Schweiger, A.; Zhang, J.; Haas, C.; et al. CryoSat-2 estimates of Arctic sea ice thickness and volume. *Geophys. Res. Lett.* **2013**, *40*, 732–737. [CrossRef]

21. Tilling, R.L.; Ridout, A.; Shepherd, A. Estimating Arctic sea ice thickness and volume using CryoSat-2 radar altimeter data. *Adv. Space Res.* **2018**, *62*, 1203–1225. [CrossRef]

22. Kwok, R.; Zwally, H.J.; Yi, D. ICESat observations of Arctic sea ice: A first look. *Geophys. Res. Lett.* **2004**, *31*, L16401. [CrossRef]

23. Kwok, R.; Cunningham, G.F. ICESat over Arctic sea ice: Estimation of snow depth and ice thickness. *J. Geophys. Res. Oceans* **2008**, *113*, C08010. [CrossRef]

24. Kacimi, S.; Kwok, R. Arctic Snow Depth, Ice Thickness, and Volume From ICESat-2 and CryoSat-2: 2018–2021. *Geophys. Res. Lett.* **2022**, *49*, e2021GL097448. [CrossRef]

25. Louet, J.; Bruzzi, S. ENVISAT mission and system. In Proceedings of the IEEE 1999 International Geoscience and Remote Sensing Symposium. IGARSS'99 (Cat. No.99CH36293), Hamburg, Germany, 28 June–2 July 1999. [CrossRef]

26. Wingham, D.J.; Francis, C.R.; Baker, S.; Bouzinac, C.; Brockley, D.; Cullen, R.; de Chateau-Thierry, P.; Laxon, S.W.; Mallow, U.; Mavrocordatos, C.; et al. CryoSat: A mission to determine the fluctuations in Earth's land and marine ice fields. *Adv. Space Res.* **2006**, *37*, 841–871. [CrossRef]

27. Abdalati, W.; Zwally, H.J.; Bindschadler, R.; Csatho, B.; Farrell, S.L.; Fricker, H.A.; Harding, D.; Kwok, R.; Lefsky, M.; Markus, T.; et al. The ICESat-2 laser altimetry mission. *Proc. IEEE* **2010**, *98*, 735–751. [CrossRef]

28. Baltazar Andersen, O.; Abulaitijiang, A.; Zhang, S.; Kildegaard Rose, S. A new high resolution Mean Sea Surface (DTU21MSS) for improved sea level monitoring. In *EGU General Assembly Conference Abstracts*; European Geosciences Union: Vienna, Austria, 2021.

29. Paul, S.; Hendricks, S.; Ricker, R.; Kern, S.; Rinne, E. Empirical parametrization of envisat freeboard retrieval of arctic and antarctic sea ice based on CryoSat-2: Progress in the ESA climate change initiative. *Cryosphere* **2018**, *12*, 2437–2460. [CrossRef]

30. Stefan, H.; Ricker, R.; Paul, S. *AWI CryoSat-2 Sea Ice Thickness, Version 2.4*; EPIC: Verona, WI, USA, 2021.

31. Cavalieri, D.J.; Parkinson, C.L.; DiGirolamo, N.; Ivanoff, A. Intersensor Calibration between F13 SSMI and F17 SSMIS for Global Sea Ice Data Records. 2012. Available online: https://ntrs.nasa.gov/citations/20120009376 (accessed on 12 April 2022).

32. Warren, S.G.; Rigor, I.G.; Untersteiner, N.; Radionov, V.F.; Bryazgin, N.N.; Aleksandrov, Y.I.; Colony, R. Snow depth on Arctic sea ice. *J. Clim.* **1999**, *12*, 1814–1829. [CrossRef]

33. Brucker, L.; Markus, T. Arctic-scale assessment of satellite passive microwave-derived snow depth on sea ice using Operation IceBridge airborne data. *J. Geophys. Res. Oceans* **2013**, *118*, 2892–2905. [CrossRef]

34. Markus, T.; Cavalieri, D.J.; Gasiewski, A.J.; Klein, M.; Maslanik, J.A.; Powell, D.C.; Boba Stankov, B.; Stroeve, J.C.; Sturm, M. Microwave signatures of snow on sea ice: Observations. *IEEE Trans. Geosci. Remote Sens.* **2006**, *44*, 3081–3090. [CrossRef]

35. Comiso, J.C. Warming trends in the Arctic from clear sky satellite observations. *J. Clim.* **2003**, *16*, 3498–3510. [CrossRef]

36. Petty, A.A.; Webster, M.; Boisvert, L.; Markus, T. The NASA Eulerian Snow on Sea Ice Model (NESOSIM) v1.0: Initial model development and analysis. *Geosci. Model Dev.* **2018**, *11*, 4577–4602. [CrossRef]

37. Alexandrov, V.; Sandven, S.; Wahlin, J.; Johannessen, O.M. The relation between sea ice thickness and freeboard in the Arctic. *Cryosphere* **2010**, *4*, 373–380. [CrossRef]

38. Farrell, S.L.; Kurtz, N.; Connor, L.N.; Elder, B.C.; Leuschen, C.; Markus, T.; McAdoo, D.C.; Panzer, B.; Richter-Menge, J.; Sonntag, J.G. A first assessment of IceBridge Snow and Ice thickness data over arctic sea ice. *IEEE Trans. Geosci. Remote Sens.* **2012**, *50*, 2098–2111. [CrossRef]

39. Timco, G.W.; Frederking, R.M.W. A review of sea ice density. *Cold Reg. Sci. Technol.* **1996**, *24*, 1–6. [CrossRef]

40. Arfeuille, G.; Mysak, L.A.; Tremblay, L.B. Simulation of the interannual variability of the wind-driven Arctic sea-ice cover during 1958–1998. *Clim. Dyn.* **2000**, *16*, 107–121. [CrossRef]

41. Comiso, J.C.; Cavalieri, D.J.; Markus, T. Sea ice concentration, ice temperature, and snow depth using AMSR-E data. *IEEE Trans. Geosci. Remote Sens.* **2003**, *41 Pt 1*, 243–252. [CrossRef]

42. Visbeck, M.H.; Hurrell, J.W.; Polvani, L.; Cullen, H.M. The North Atlantic oscillation: Past, present, and future. *Proc. Natl. Acad. Sci. USA* **2001**, *98*, 12876–12877. [CrossRef]
43. Kalnay, E.; Kanamitsu, M.; Kistler, R.; Collins, W.; Deaven, D.; Gandin, L.; Iredell, M.; Saha, S.; White, G.; Woollen, J.; et al. The NCEP/NCAR 40-year reanalysis project. *Bull. Am. Meteorol. Soc.* **1996**, *77*, 437–472. [CrossRef]
44. Faugere, Y.; Dorandeu, J.; Lefevre, F.; Picot, N.; Femenias, P. Envisat Ocean Altimetry Performance Assessment and Cross-calibration. *Sensors* **2006**, *6*, 100–130. [CrossRef]
45. Wingham, D.J.; Rapley, C.G.; Griffiths, H. New Techniques in Satellite Altimeter Tracking Systems. In Proceedings of the Digest—International Geoscience and Remote Sensing Symposium (IGARSS), Zürich, Switzerland, 8–11 September 1986.
46. Kwok, R.; Petty, A.; Bagnardi, M.; Wimert, J.T.; Cunningham, G.F.; Hancock, D.W.; Ivanoff, A.; Kurtz, N. *Algorithm Theoretical Basis Document (ATBD) for Sea Ice Products*; National Aeronautics and Space Administration: Washington, DC, USA, 2022.
47. Pukelsheim, F. The three sigma rule. *Am. Stat.* **1994**, *48*, 88–91. [CrossRef]
48. Ollivier, A.; Faugere, Y.; Picot, N.; Ablain, M.; Femenias, P.; Benveniste, J. Envisat Ocean Altimeter Becoming Relevant for Mean Sea Level Trend Studies. *Mar. Geod.* **2012**, *35* (Suppl. 1), 118–136. [CrossRef]
49. Kwok, R.; Cunningham, G.F.; Zwally, H.J.; Yi, D. Ice, Cloud, and land Elevation Satellite (ICESat) over Arctic sea ice: Retrieval of freeboard. *J. Geophys. Res. Oceans* **2007**, *112*, C12013. [CrossRef]
50. Farrell, S.L.; Laxon, S.W.; McAdoo, D.C.; Yi, D.; Zwally, H.J. Five years of arctic sea ice freeboard measurements from the ice, cloud and land elevation satellite. *J. Geophys. Res. Oceans* **2009**, *114*, C04008. [CrossRef]
51. Beaven, S.G.; Lockhart, G.L.; Gogineni, S.P.; Hosseinmostafa, A.R.; Jezek, K.; Gow, A.J.; Perovich, D.K.; Fung, A.K.; Tjuatja, S. Laboratory measurements of radar backscatter from bare and snow-covered saline ice sheets. *Int. J. Remote Sens.* **1995**, *16*, 851–876. [CrossRef]
52. Agarwal, P.K.; Avraham, R.; Ben Kaplan, H.; ShCPir, M. Computing the discrete fréchet diStance in subquadratic time. *SIAM J. Comput.* **2014**, *43*, 429–449. [CrossRef]
53. Landy, J.C.; Dawson, G.J.; Tsamados, M.; Bushuk, M.; Stroeve, J.C.; Howell, S.E.L.; Krumpen, T.; Babb, D.G.; Komarov, A.S.; Heorton, H.D.B.S.; et al. A year-round satellite sea-ice thickness record from CryoSat-2. *Nature* **2022**, *609*, 517–522. [CrossRef]
54. Li, M.; Luo, D.; Simmonds, I.; Dai, A.; Zhong, L.; Yao, Y. Anchoring of atmospheric teleconnection patterns by Arctic Sea ice loss and its link to winter cold anomalies in East Asia. *Int. J. Climatol.* **2021**, *41*, 547–558. [CrossRef]
55. Hilmer, M.; Lemke, P. On the decrease of Arctic Sea ice volume. *Geophys. Res. Lett.* **2000**, *27*, 3751–3754. [CrossRef]
56. Schweiger, A.J.; Wood, K.R.; Zhang, J. Arctic Sea Ice volume variability over 1901–2010: A model-based reconstruction. *J. Clim.* **2019**, *32*, 4731–4752. [CrossRef]